CHEMISTRY OF MATERIALS
Cite This: Chem. Mater. 2019, 31, 3239−3247
Article
pubs.acs.org/cm

Monitoring the Electrochemical Energy Storage Processes of an Organic Full Rechargeable Battery via Operando Raman Spectroscopy: A Mechanistic Study

Xiu-Mei Lin,*[,†,‡] De-Yin Wu,*[,§] Ping Gao,[†] Zhi Chen,[∥] Mario Ruben,[∥] and Maximilian Fichtner*[,†,∥]

[†]Helmholtz Institute Ulm for Electrochemical Energy Storage (HIU), Helmholtzstr 11, 89081 Ulm, Germany
[‡]Department of Physics and [§]State Key Laboratory of Physical Chemistry of Solid Surfaces, iChEM, College of Chemistry and Chemical Engineering, Xiamen University, 361005 Xiamen, China
[∥]Institute of Nanotechnology, Karlsruhe Institute of Technology (KIT), P.O. Box 3640, 76021 Karlsruhe, Germany

Supporting Information

ABSTRACT: The green, sustainable, and versatile nature of using organic compounds that can be derived from biomass makes them extremely interesting materials for use in various rechargeable batteries. However, the overall electrochemical reaction mechanism of an organic full rechargeable battery has seldom been reported because of the lack of straightforward and accessible analytical techniques that capable of probing the rechargeable battery system in real time. Herein, we configured an organic full rechargeable battery composed of a porphyrin−metal complex [5,15-bis-(ethynyl)-10,20-diphenylporphinato]copper(II) (CuDEPP) anode, a graphite cathode, and a 1-butyl-1-methylpiperidinium bis-(trifluoromethanesulfonyl)imide (PP14TFSI) ionic liquid electrolyte. Operando Raman spectroscopy was employed to simultaneously monitor the evolution of Raman bands from the anode, cathode, and electrolyte of the battery caused by electrochemical energy storage (EES) processes. It was found that during EES processes, the electronic structural changes of the CuDEPP anode mainly occurred at the porphyrin ring and ethynyl substituent rather than at the Cu(II) metal center and benzene substituent, followed by interactions with $PP14^+$ cations of the electrolyte. Also, complementary density functional theory (DFT) calculations on the anode redox reaction mechanism were performed and support the spectroscopic results. Meanwhile, during EES processes at the cathode, $TFSI^-$ anions intercalated into/deintercalated out of the graphite cathode, which resulted in the appearance and disappearance of a G′ spectral band at 1610 cm^{-1}. Our findings suggest the conjugated porphyrin ring and ethynyl substituent of the organic anode have a beneficial redox effect that supports charge−discharge cycling and reveals the interactions between the electrodes and electrolytes for the better design of organic EES devices.

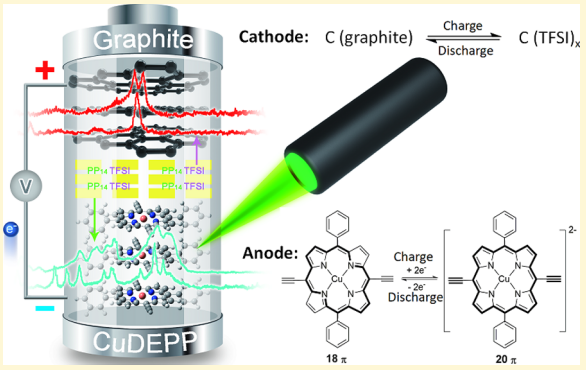

1. INTRODUCTION

Modern societies' rapid technological advancements necessitate higher requirements from state-of-the-art rechargeable battery systems in not only electrochemical performance but also resource sustainability and environmental friendliness.[1−6] Conventional rechargeable batteries based on inorganic materials offer high-energy densities but are limited by slow charge/discharge kinetics and the depletion of resources.[7,8] Organic materials can achieve high rates due to the electrochemical redox reactions, which bypass intercalation and solid-state diffusion limitations. Moreover, they can be obtained from natural biomass with minimum energy consumption. Therefore, they are an attractive affordable and sustainable choice for battery electrode materials.[1−3]

Although many organic electrode materials with various molecular structures have been investigated as cathodes or anodes for various rechargeable batteries with high electrochemical performance, many of their reaction mechanisms remain ambiguous. For example, the reversible redox reactions of electrode molecules are often presumed based on predictions without any real-time experimental monitoring. Therefore, the changes in the electronic structure of specific organic groups or moieties contributing to the EES processes of the organic electrodes are often unclear. Also, many mechanistic studies of organic electrodes are performed in half-cell, not full-cell, configurations. In addition, they use Li or Na metal as a counter electrode to study the reaction mechanism of only the organic working electrode. To the best of our knowledge, the overall reaction mechanism during the EES processes of full rechargeable batteries, including dynamic

Received: January 8, 2019
Revised: April 10, 2019
Published: April 11, 2019

Downloaded via KIT BIBLIOTHEK on July 29, 2019 at 14:00:47 (UTC).
See https://pubs.acs.org/sharingguidelines for options on how to legitimately share published articles.

© 2019 American Chemical Society

DOI: 10.1021/acs.chemmater.9b00077
Chem. Mater. 2019, 31, 3239−3247

redox, intercalation, and alloying reactions on both anode and cathode, and interaction between the electrodes and the electrolyte have not been reported until now. A thorough mechanistic understanding of the EES processes of organic full rechargeable batteries is of great significance for optimizing their properties and improving electrochemical performance also, which is the key to their development.

So far, the electrochemical reaction mechanisms of some organic battery materials in half-cells have been investigated by different methods.[6,9−16] The superlithiation behavior of dilithium benzenedipropiolate[6] and the sodium storage mechanism in disodium terephthalate ($C_8H_4Na_2O_4$)[9] were investigated using DFT calculations. In the past few years, disodium rhodizonate ($Na_2C_6O_6$) was reported as an anode material for sodium-ion batteries with a 501 mAh g^{-1} theoretical capacity based on presumed four-electron redox chemistry from different groups.[10−12] Its four-sodium storage mechanism was recently revealed using operando X-ray diffraction (XRD).[13] Poly(anthraquinonyl sulfide) (PAQS) was used as a cathode material in lithium-ion[14] and magnesium-ion[15] batteries in 2009 and 2015, respectively. Recently, its electrochemical reaction mechanism was investigated by operando infrared (IR) spectroscopy.[16] All these techniques have provided important information to understand the reaction mechanism of the organic electrode materials. However, it should be noted that XRD can only provide the structural information for crystalline materials; therefore, its applications to amorphous raw materials or intermediates studies are limited. While the IR signal of samples is interfered by an aqueous solution, hence its applications in batteries with aqueous electrolytes are limited.

Complementarily, Raman spectroscopy can provide fingerprint vibrational information from molecular or lattice vibrations of both crystalline and amorphous materials in air, aqueous solutions, or organic solvents.[17−19] Different intermediates produced during battery cycling processes are often easily hydrolyzed or oxidized in atmosphere, making operando characterization techniques indispensable for investigating battery reaction mechanisms.[20] Operando Raman characterization and monitoring of electrode materials can be achieved by coupling a battery cycling system to a Raman instrument via an air-tight electrochemical Raman cell, enabling changes in the charge state and electronic structure of electrode materials to be detected during EES processes by observing changes in distinctive vibrational modes. Furthermore, the formed intermediates and reaction mechanisms can be elucidated. This technique has been used to investigate the cycling behavior of carbon,[21−25] sulfur,[26,27] and metal oxide electrodes.[28−30]

Porphyrin−metal complexes are ubiquitous in nature and have become the target of active investigations in the life sciences,[31] catalyses,[32−34] and especially rechargeable EES devices[35−39] owing to their attractive molecular and electronic properties. They generally have small energy gaps between the highest occupied molecular orbital (HOMO) and the lowest unoccupied molecular orbital (LUMO) that enable the facile injection and removal of electrons, thus leading to fast bipolar redox kinetics.[40,41] In this report, we configured an organic full rechargeable battery composed of a porphyrin−metal complex CuDEPP anode, a graphite cathode, and a PP14TFSI ionic liquid electrolyte and used operando Raman spectroscopy to monitor its EES processes. The chosen of the configuration is regarding on the CuDEPP anode, graphite cathode, and PP14TFSI electrolyte that are all Raman active; hence, the Raman spectroscopic investigations on the overall operation mechanism of the full battery are probable. The battery performance has been briefly reported elsewhere,[35] but the reaction mechanism has not been investigated. Herein, rather than presenting a new battery material, we used the porphyrin−metal complex cell as a model system to reveal the overall reaction mechanism of an organic full rechargeable battery.

During charging of the battery, we found that the Raman peaks originating from the conjugated porphyrin ring and ethynyl substituent of the CuDEPP anode varied dramatically. However, at the end of discharging of the battery, the changes were nearly completely reversed. In strong contrast, the Raman peaks from the central Cu−N bond and benzene substituent remained relatively constant throughout charge−discharge cycling, indicating that the reversible two one-electron electrochemical redox reaction on the CuDEPP anode changes the electronic structure of the former rather than the latter. Combined DFT calculations show that the frontier orbitals of the CuDEPP are mainly related to the orbitals of the porphyrin ring and the ethynyl group, whereas the contribution from the central Cu atom and benzene group is small and can be ignored, complementing the experimental results. Moreover, during charging, the $PP14^+$ cations of the electrolyte migrated to $[CuDEPP]^{2-}$ to compensate for its negative charge and migrated back to the electrolyte during discharge. This was observed in the Raman spectra by the variations in the Raman signal intensity of $PP14^+$ cations. Meanwhile, the Raman spectra of the cathode during charging revealed the intercalation of $TFSI^-$ anions into the graphite cathode, resulting in a new G′ band appearing at 1610 cm^{-1}. The G′ band then disappeared on discharging when the $TFSI^-$ anions deintercalated out of the cathode and migrated back into the electrolyte.

2. EXPERIMENTAL SECTION

2.1. Materials. [5,15-Bis(ethynyl)-10,20-diphenylporphinato]-copper(II) (CuDEPP) was synthesized as reported[35] and dried at 100 °C for 12 h under vacuum before use. Commercial graphite (Sigma-Aldrich) was dried at 200 °C for 12 h under vacuum. The 1-butyl-1-methylpiperidinium bis(trifluoromethylsulfonyl)imide (PP14TFSI, 99.9%) ionic liquid electrolyte for the CuDEPP/PP14TFSI/graphite cell was purchased from Iolitech GmbH and was dried at 85 °C for 72 h under vacuum. Other reagents were purchased from InnoChem Science & Technology Co., Ltd., and were used as received.

2.2. Electrochemical Investigation. Cyclic voltammetry (CV) experiments were carried out on a potentiostat/galvanostat using a standard three electrodes setup with a glassy carbon disk working electrode (2 mm diameter), a Ag/Ag^+ reference electrode, and a Pt wire counter electrode. The supporting electrolyte was 0.1 M TBAP in CH_2Cl_2. The scan range was from −1.95 to +1.80 V and the scan rate was 50 mV s^{-1}.

2.3. Charging/Discharging Tests. Charge/discharge cycling tests were performed using a 2032 coin-type cell (Hohsen Corp., Japan) constructed in an Ar glovebox (0.1 ppm O_2 and H_2O). Glass fiber filters (GF/D, Whatman) were used as separators. The CuDEPP electrode was prepared by grinding a mixture of CuDEPP, carbon black, and polyvinylidene fluoride (PVDF) binder in a weight ratio of 50:40:10 in *N*-methyl-2-pyrrolidone (NMP) solvent to form the electrode slurry. For graphite electrodes, the weight ratio of each was 85:5:10. The resulting slurries were spread on stainless current collectors (16 mm dia.) and dried in a vacuum oven at 100 °C for 12 h. Typically, each electrode contained about 2.0 mg of the active material. The electrolyte was PP14TFSI ionic liquid. Charge and

DOI: 10.1021/acs.chemmater.9b00077
Chem. Mater. 2019, 31, 3239−3247

discharge measurements were performed with an Arbin BT2000 battery system at 298 K.

2.4. Operando Raman Investigations. The complete operando electrochemical Raman system was built by connecting an operando electrochemical Raman cell (EL-CELL, GmbH) to a Raman instrument (InVia, Renishaw) using a Gamry Interface1000 potentiostat to cycle the constructed batteries as shown in Figure S1.

The construction procedure (see Figure 1) of the battery in the Raman cell for operando investigations was similar to that in the coin cell but with a 1 mm-diameter hole in the center of the current collector to allow Raman laser illumination and signal collection from the back side of the cell. The two electrodes cell was configured from top to bottom with the counter electrode at the spring-loaded piston, followed by the glass fiber separator, electrolyte, and then the working electrode. The cell was then sealed to the atmosphere with a thin optical quartz window (0.15 mm) and made air-tight with a rubber seal, enabling nonaqueous electrochemical processes to be investigated operando.

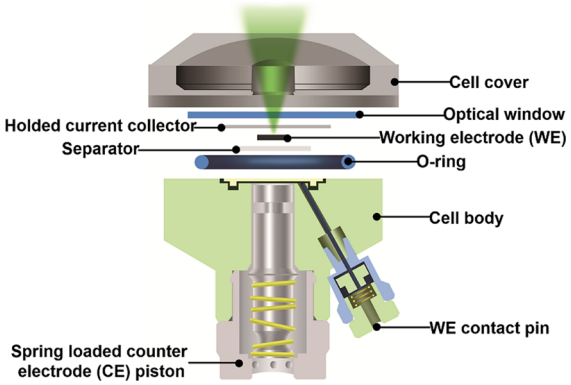

Figure 1. Scheme of the operando electrochemical Raman spectroscopic cell.

The operando Raman cell was then removed from the glovebox, positioned atop the Raman microscope stage, and connected to the potentiostat. Raman spectra were recorded at room temperature (about 25 °C) with a confocal Raman microscope using a laser with a wavelength of 532 nm as the excitation source. The laser power was ~1.0 mW. The spectral acquisition time was 5–20 s, depending on different samples.

2.5. Computational Details. Density functional theory (DFT) calculations were carried out with hybrid exchange-correlation functional B3LYP. To mimic the electronic structures of porphyrin–copper complex, we considered there are three charged states, $[PPy–Cu]^0$, $[PPy–Cu]^{1-}$, and $[PPy–Cu]^{2-}$. The basis sets for C, N, and H atoms of studied molecules were 6-311+G(d,p), which includes a polarization function to all five kinds of atoms and a diffuse function to C, N, and H atoms. For the Cu atom, electrons in the valence and inner shells were described by the basis set, LANL2DZ, and the corresponding relativistic effective core potentials, respectively. Full geometric optimization was carried out by using Gaussian 09 package.

3. RESULTS AND DISCUSSION

3.1. Redox Activity of the CuDEPP Complex and its Performance as an Anode in an Organic Full Rechargeable Battery. The structural formula of CuDEPP is shown in Figure 2a, and its bipolar redox-activity was first examined by cyclic voltammetry (CV). As shown in Figure 2b, four reversible one-electron transfer reactions were visible at −1.88 (peak 1′), −1.00 (peak 2′), 0.49 (peak 3′), and 1.06 V (peak 4′) versus Ag/Ag^+ in a tetrabutylammonium perchlorate/dichloromethane ($TBAP/CH_2Cl_2$) supporting electrolyte. These four reactions include two one-electron reduction and two one-electron oxidation processes at the conjugated porphyrin complex to give a porphyrin anion radical and dianion or cation radical and dication. Note that the reduction peak of 4′ and oxidation peaks of 1 and 2 are not as noticeable as other peaks, which may be due to the instability of the intermediates at these potentials. Therefore, operando characterization is crucial for the material.

In this study, we only utilized the reduction reactions of the CuDEPP complex and coupled it with a graphite cathode and PP14TFSI electrolyte to configure an organic full rechargeable battery[35] as illustrated in Figure 3a. The galvanostatic tests for the battery were carried out at an operating voltage between 4.0 and 0.0 V with a specific current of 2 A g^{-1} (~21 C) to clarify the electrochemical behavior of the battery and to correlate the operando Raman measurements later on. For all the battery performance tests and operando measurements, the voltage of the full battery is the potential difference between the CuDEPP anode and graphite cathode. As can be seen in Figure 3b, the initial charging shows a flat voltage plateau at about 3.2 V, but no well-defined voltage plateau is present in the successive charge/discharge profiles, thus indicating rapid multiple redox reactions without clear phase transitions.[35] Discharge capacities of 72, 69, and 68 mA h g^{-1} were obtained at 1st, 2nd, and 3rd cycles, indicating a highly reversible discharge/charge event. The selected charge–discharge curves at 100th, 200th, 300th, and 400th in Figure 3c show only slightly decreased capacity with increasing cycles. The capacity retention is about 85% for the first 2000 cycles as shown in the

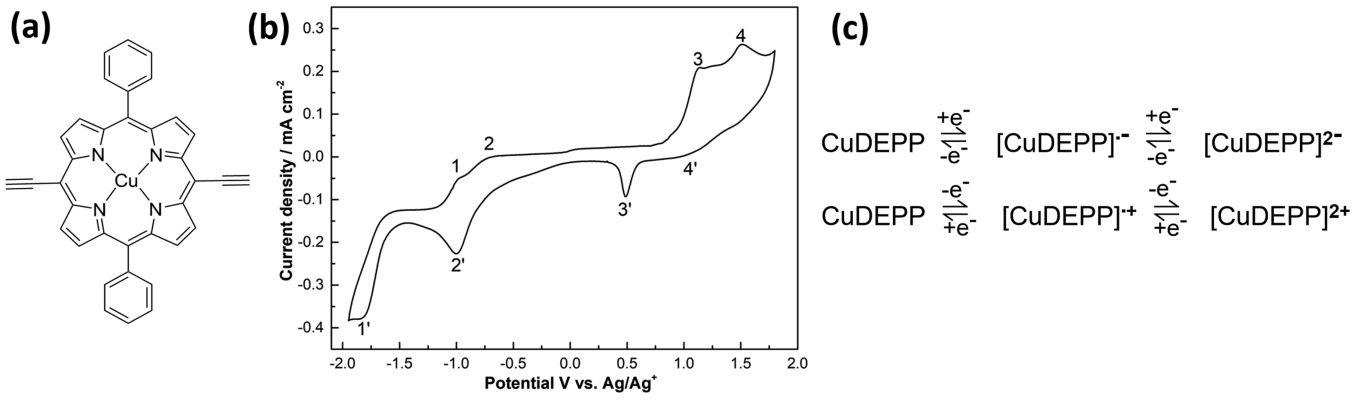

Figure 2. (a) Structural formula of CuDEPP. (b) CV of 1 mM CuDEPP in a 0.1 M $TBAP/CH_2Cl_2$ supporting electrolyte/solvent with a 50 mV s^{-1} scan rate. (c) Two one-electron reduction and two one-electron oxidation reactions of CuDEPP.

DOI: 10.1021/acs.chemmater.9b00077
Chem. Mater. 2019, 31, 3239–3247

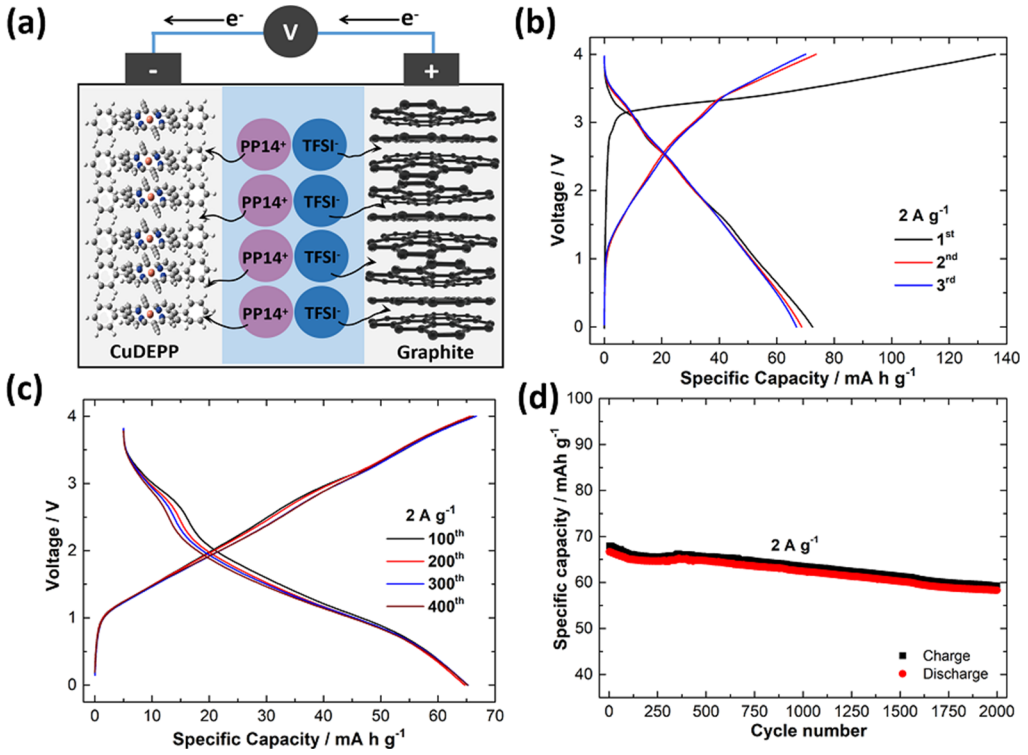

Figure 3. (a) Configuration of CuDEPP/PP14TFSI/graphite organic full rechargeable battery. (b) Selected galvanostatic charge−discharge profiles for the 1st, 2nd, and 3rd cycles. (c) Selected galvanostatic charge−discharge profiles for the 100th, 200th, 300th, and 400th cycles. (d) "Capacity vs cycle number" plot for 2000 cycles. The specific capacity was calculated according to the mass of CuDEPP (50 wt % of the total electrode) and was subjected to a specific current of 2 A g^{-1}.

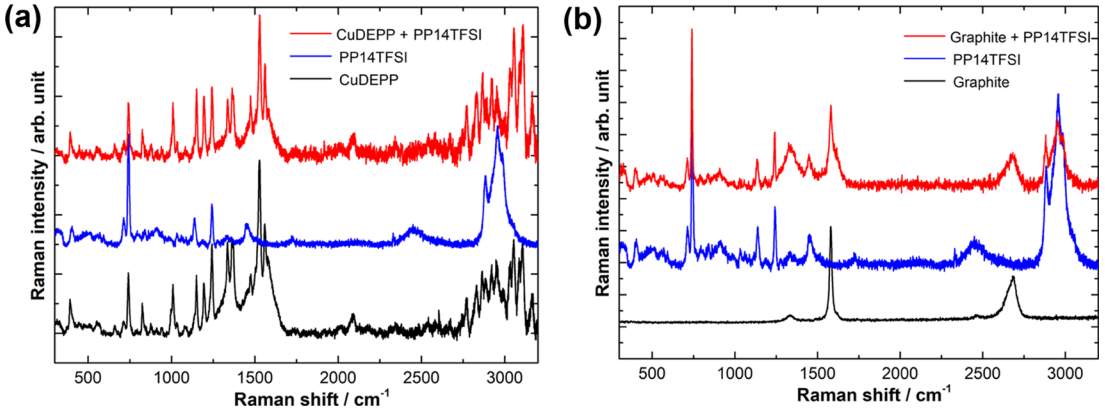

Figure 4. Raman spectra of (a) CuDEPP, PP14TFSI, and CuDEPP and PP14TFSI. (b) Graphite, PP14TFSI, and graphite and PP14TFSI.

long-term cycling performance test in Figure 3d. Accordingly, a specific energy of ∼163 Wh kg^{-1} at a specific power of ∼32.6 kW kg^{-1} is observed. The theoretical capacity is about 93.7 mA h g^{-1} according to the two-electron reduction reaction of CuDEPP to $[CuDEPP]^{2-}$ as calculated in the Supporting Information. Although the specific capacity is limited by the relatively high-molecular weight of the complex, it shows good cycle stability with fast charge/discharge kinetics and reasonable energy and power densities. Therefore, it serves as a good model system to study the overall reaction mechanism of an organic full rechargeable battery from the spectroscopic and electrochemical performance aspects.

3.2. Raman Spectra of the Electrodes and Electrolyte. To add clarity to the operando Raman spectra and peak changes, Raman spectra of electrodes and electrolytes were first measured for comparison. The Raman spectra of CuDEPP anode, electrolyte, and CuDEPP+PP14TFSI are shown in Figure 4a. The CuDEPP anode and PP14TFSI electrolyte show their distinctive Raman spectra, whereas the Raman spectra of CuDEPP and PP14TFSI only show spectral features from the CuDEPP. This is due to the resonance Raman effect of CuDEPP under the excitation of the 532 nm incident laser. The UV−Vis adsorption spectra of CuDEPP (Figure S2) has an adsorption peak at 555 nm, which is close to the 532 nm excitation laser and induces the resonance Raman effect on CuDEPP.[43−47] Therefore, the CuDEPP shows a much stronger Raman signal than the PP14TFSI ionic liquid and covers the latter's Raman signal. Figure 4b shows the Raman spectra of the graphite cathode, PP14TFSI electrolyte, and the graphite+PP14TFSI. The graphite cathode and PP14TFSI

DOI: 10.1021/acs.chemmater.9b00077
Chem. Mater. 2019, 31, 3239−3247

electrolyte show their specific Raman spectra, whereas the Raman spectrum of graphite and PP14TFSI shows the spectral features from both components because of their comparable signal intensities.

3.3. Reduction Behavior of Organic CuDEPP Anode Investigated by Combined Operando Raman Spectroscopy and DFT Calculations. Figure 5 shows the dynamic

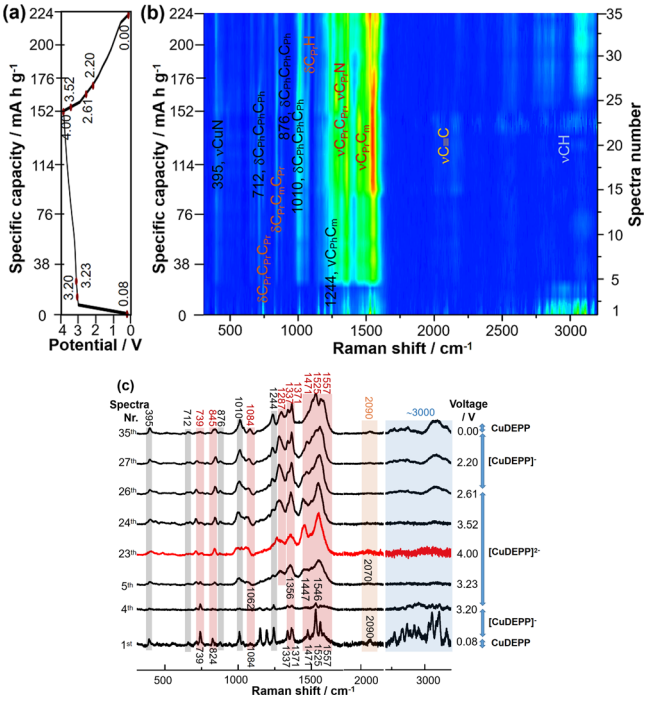

Figure 5. Dynamic spectral evolution of the CuDEPP anode during the initial cycling at a current density of 0.5 A g^{-1}. (a) Voltage profile. (b) Capacity-dependent operando Raman spectral contour plots with main peaks assignment. (c) Selected Raman spectra corresponding to (a) and (b). C_{Pr}: pyrrole carbons, C_{Ph}: phenyl carbons, C_m: methine bridge carbons, ν: stretching, δ: in-plane deformation.

spectral evolution of the CuDEPP anode during the first charge−discharge cycle at a specific current of 0.5 A g^{-1}. Additionally, a series of all collected Raman spectra with full spectral ranges from 300 to 3200 cm^{-1} at corresponding potentials are provided in Figure S3. The assignments of the spectra[41−47] are provided in Table S1 and are also appended on respective peaks in Figure 5b. Compared to the battery performance tests, a smaller specific current (2.0 A g^{-1} vs 0.5 A g^{-1}) was applied to cycle the battery for having sufficient time for a detailed spectra acquisition during the operando Raman measurement. As shown in Figure S4, the galvanostatic profiles of the battery at 2.0 and 0.5 A g^{-1} for the first cycle are similar, although their cycling times are different (31 vs 122 min). In our measurements, grating of the spectrometer has to be automatically rotated for two times to obtain one full-range Raman spectrum (300−3200 cm^{-1}), which takes a few minutes.

In Figure 5a−c, at the initial charging stage from OCV at 0.08−3.20 V, with the potential increasing, spectra (Nr. 1st−4th) show similar vibrational features as the pristine CuDEPP electrode, although the intensity gradually decreases until almost disappears. From 3.20−3.23 V, spectra (Nr. 4th−5th) dramatically change at both vibration modes and peak intensity, especially in the spectral ranges of ∼1100−1600 cm^{-1} and ∼3000 cm^{-1}. During the successive charging from 3.23 to 4.00 V and then discharging from 4.00 to 2.61 V, spectra at different potentials (Nr. 5th−26th) show similar vibrational feature, although the intensity of some vibration modes vary. After 2.61 V, spectra gradually convert back to the original OCV spectral state by the end of discharging at 0.00 V (Nr. 27th−35th).

Accordingly, as shown in Figure 5c, it seems that during charging, the CuDEPP anode was reduced to $[CuDEPP]^-$ as soon as the charging started and stayed at this state until ∼3.20 V and then was further reduced to $[CuDEPP]^{2-}$ after 3.20 V and stayed until 4.00 V. During discharging, the $[CuDEPP]^{2-}$ state was kept from 4.00 to ∼2.61 V and then was oxidized to $[CuDEPP]^-$ after 2.61 V and was finally oxidized to CuDEPP at 0.00 V. This is consistent with the two one-electron reduction reactions of the CuDEPP as shown in Figure 2b,c.

Further, detailed analysis on the series of Raman spectra peak assignments shows that vibrational modes arising from the porphyrin ring and ethynyl substituent (Figure 5b,c marked and highlighted in red and orange, respectively) vary greatly with potential, whereas other vibration modes are relatively stable. During cycling, the $C_{Pr}C_{Pr}C_{Pr}$ deformation peak position at 739 cm^{-1} remains constant, although its intensity varies greatly. The $C_{Pr}C_mC_{Pr}$ deformation peak intensity is relatively constant, whereas its position shifts during cycling, from 824 to 845 cm^{-1}. Also, the $C_{Pr}C_{Pr}$ stretching peak position shifts from 1471 to 1447 cm^{-1} and shifts back again to 1471 cm^{-1}. Different $C_{Pr}C_{Pr}$ stretching modes at 1337 and 1371 cm^{-1} merge into one peak at 1356 cm^{-1}, and different $C_{Pr}C_m$ stretching modes at 1525 and 1557 cm^{-1} merge into one peak at 1546 cm^{-1} from 3.23 V until the end of the charging, while they each gradually splits back into two respective peaks during discharging, indicating a reversible process. The C≡C stretching shifts from 2090 to 2070 cm^{-1} during charging and then shifts back to 2090 cm^{-1} at the end of discharging. In strong contrast, Cu−N stretching at 395 cm^{-1} maintains both constant peak position and intensity throughout cycling. Moreover, vibrational modes attributed to the deformation of substituent benzene ($\delta C_{Ph}C_{Ph}C_{Ph}$) at 712, 876, and 1010 cm^{-1}, and the $C_{Ph}C_m$ stretching at 1244 cm^{-1} are also relatively stable throughout cycling. Vibration modes of Cu−N and substituent benzene rings are marked in black in Figure 5b and highlighted in gray in Figure 5c.

These variations in the Raman spectra (peak positions and intensities) of the CuDEPP anode during charge−discharge cycling are due to the redox reactions induced by changes in electrode potential, resulting in the changes in the electronic structure of the CuDEPP molecule. The electronic structure of low-valent metal (M; where M = Fe, Co, Ni, Cu, or Zn)−porphyrin complexes has been studied for decades,[41−47] especially for Fe(II)−porphyrin complexes due to their biological importance. Fe(II)−porphyrin complexes have been theoretically studied previously using DFT simulations[41] and experimentally investigated by a variety of spectroscopic techniques including UV−Vis,[43] resonance Raman,[44] and deuterium NMR spectroscopy.[48] Studies show that adding an electron to a four-coordinate Fe(II)-porphyrin complex either reduces the Fe(II) metal center to Fe(I) or the porphyrin ligand to the p-anion (or a combination of both). The addition of a second electron leads to additional possibilities (Fe(0), Fe(I)−p−anion or Fe(II)-dianion), which is highly dependent upon the relative electron withdrawing capabilities of the porphyrin macrocycle and the

DOI: 10.1021/acs.chemmater.9b00077
Chem. Mater. 2019, 31, 3239−3247

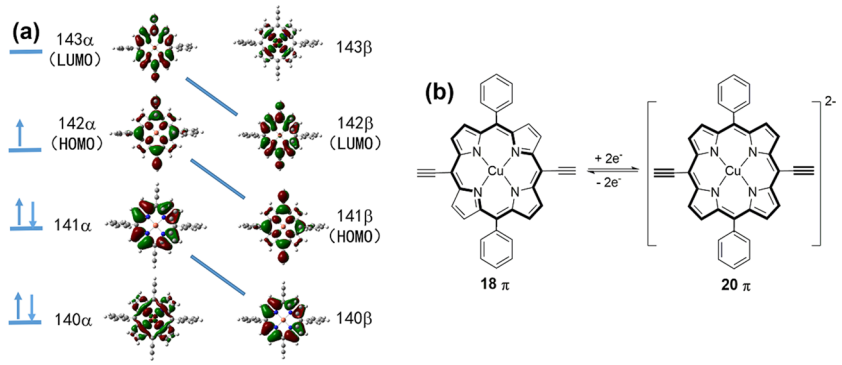

Figure 6. (a) Electron configuration and related frontier molecular orbital of the neutral CuDEPP compound. (b) The two-electron reduction of the CuDEPP mainly changes the charge state/electronic structure of the porphyrin ring and ethynyl groups. The bold line on the porphyrin ring indicates each p-conjugation circuit.

central metal, and is also influenced by the peripheral substituents of the porphyrin complexes.[41−47] Conclusions from different studies are still inconsistent. Studies on Cu(II)−porphyrin complexes are fewer than to Fe(II)−porphyrin complexes. However, existing simulations indicate that the first redox reaction in porphyrin complexes with Cu occurs at the ligand and the Cu(II) metal center remains in its initial oxidation state.[32,49]

On the basis of the above analysis, a rational explanation for the operando evolution of spectral bands in Figure 5 would be that the reduction reaction causes changes in the electronic structure of the porphyrin ring and ethynyl substituent rather than the central Cu metal and substituent benzene. Namely, porphyrin is reduced to the p-anion when an electron is electrochemically added and is reduced to the p-dianion when the second electron is added, while the oxidation state of the Cu(II) metal center remains unchanged. This avoids the collapse of the CuDEPP molecular structure being induced by the redox reaction of the central metal, which has beneficial effects on maintaining the cycling stability of the anode. Moreover, because of the strong electron withdrawing ability, the reduction reaction also increases the charge density on the C≡C bond,which is supported by the shifting of the C≡C stretching from 2090 to 2070 cm^{-1} during charging. Furthermore, previous reports show the beneficial effects of terminal ethynyl groups on the electronic conductivity and electrochemistry of porphyrins.[49,50] The changes on the electronic structure of the porphyrin−metal complex as a whole changes its resonance state also; hence, resulting in the variation of the Raman peaks of different C−H vibrations in the spectral range of ∼2500−3200 cm^{-1}.

Figure 6a shows the electron configuration and related frontier molecular orbital diagram of the neutral CuDEPP complex calculated by density functional theory (DFT), which has an unpaired electron. The α and β spin orbitals are given. As can be seen from the figure, the frontier orbitals are mainly related to the orbitals of the porphyrin ring and ethynyl substituent, whereas the contributions from the central Cu atom and the benzene substituent are negligible and can be ignored. This is consistent with the experimentally observed results. Combining the experimental results and the simulation data, the reduction and reversible oxidation reaction mechanisms of the CuDEPP anode, which contribute to the electrochemical energy storage and affects the spectral character of the molecule, are illustrated in Figure 6b.

Note that the Raman peaks of the pristine CuDEPP anode are sharp. However, these peaks broaden during charging, especially for the bands in the ∼1100−1600 cm^{-1} and ∼3000 cm^{-1} spectral ranges. This can be attributed to the interaction of $PP14^+$ cations with the CuDEPP material, which results in increased coherent scattering of light on the material. During discharging, these Raman peaks gradually get sharper again, but they remain broader than pristine CuDEPP. For instance, the νC−H vibrational peaks remain merged together, forming a broad ridge. Moreover, the changes on few peaks are irreversible. We attribute these spectral features to a slightly irreversible recovery in the CuDEPP molecular structure, which lead to tiny irreversible energy losses in the material.

3.4. Interaction between the Electrodes and Ionic Liquid Electrolyte Revealed by Operando Raman Spectroscopy on Graphite Cathode. To explore the reactivity on the cathode and to investigate the operation mechanism of the complete battery, we performed operando Raman measurement on the graphite also, see Figure 7. Additionally, a series of Raman spectra with full spectral ranges from 300 to 3200 cm^{-1} at corresponding potentials are provided in Figure S5. As can be seen in Figure 7b,c, the initial Raman spectra show three vibration bands belong to graphite: the D, G, and 2D bands at 1340, 1585, and 2680 cm^{-1}, respectively (marked and highlighted in red).[21−25] During charging from OCV at 0.08 to 3.23 V, spectra (Nr. 1st−4th) show no obvious changes on the graphite bands. During the subsequent charging, a new tiny peak at 1610 cm^{-1} (G′ band) appears at 3.26 V, and its intensity gradually increases until the end of the charging at 4.00 V. During discharging, the intensity of the G′ band decreases until completely disappears by the finishing of the first cycle. In contrast to the G′ band, the intensity of the G band decreases while the charging and growing back during the following discharging.

The G band is attributed to the stretching modes of sp^2-C atoms in the pure graphite material. When ions intercalate into graphite, a graphite intercalation compound (GIC) is formed, which shows an extra G′ band at 1610 cm^{-1}. Two kinds of graphene layer planes are present in GIC, interior (not adjacent to the intercalate layers) and bounding (adjacent to the intercalate layers), and these exhibit a doublet structure in the Raman spectra of graphite cathode. The intensity of the G band from interior graphene layers decreases as the concentration of intercalated species in the graphite host increases. Whereas, the intensity of the G′ band of the bounding graphene layers increases as the concentration of

DOI: 10.1021/acs.chemmater.9b00077
Chem. Mater. 2019, 31, 3239−3247

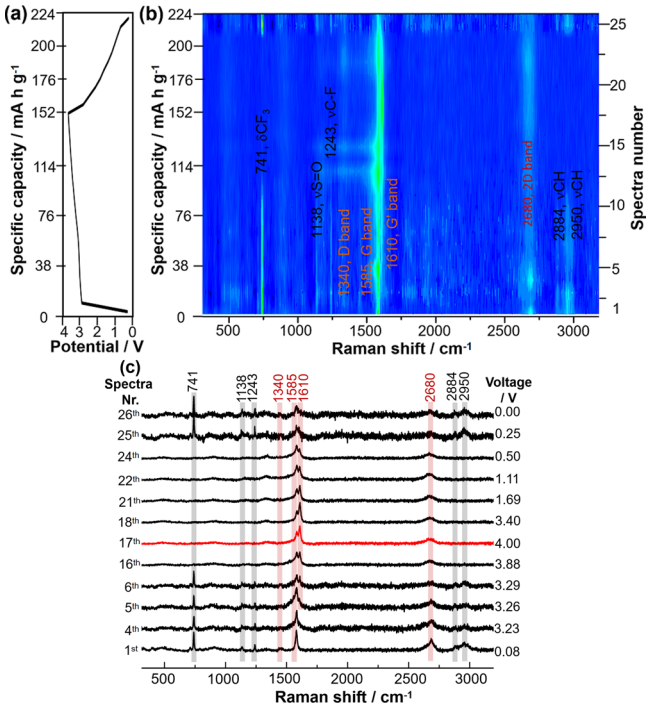

Figure 7. Dynamic spectral evolution of the graphite cathode during the initial cycling at a current density of 0.5 A g^{-1}. (a) Voltage profile. (b) Capacity-dependent operando Raman spectral contour plots. (c) Selected Raman spectra corresponding to (a) and (b). ν: stretching, δ: in-plane deformation.

intercalates increases.[30−34] Accordingly, during charging, to compensate for the positive charges generated on the cathode, $TFSI^-$ anions start migrating and intercalating into graphite at ~3.26 V, and then deintercalate out of the host graphite and migrate back to the electrolyte during the discharging. The phenomenon of $TFSI^-$ intercalation into graphite is similar to the intercalation of other anions into graphite as reported previously, both show the formation of the G band doublet.[51,52]

Note that apart from the vibrational modes from the graphite cathode, due to the comparable signal intensities of graphite and PP14TFSI, the initial operando Raman spectrum shows five other spectral bands belonging to the electrolyte (Figure 7b marked in black and Figure 7c highlighted in gray). The molecular structure of PP14TFSI is shown in Figure S6a. These five bands are also marked on the Raman spectrum of the pure PP14TFSI ionic liquid electrolyte in Figure S6b. Interestingly, the interactions between the electrode and relevant electrolyte ions can be observed throughout the operando Raman spectra also. As shown in Figure 7a−c, during charging, the intensity of the νCH bond vibrations of $PP14^+$ cations at 2884 and 2950 cm^{-1} decreases as soon as the external circuit was added. It indicates that the cations are expelled from the cathode surface because of double layer reordering and columbic repulsion with the increasingly positive graphite cathode surface and are replaced with $TFSI^-$ anions. The $PP14^+$ cations then migrate to the anode to neutralize negative charges of the $[CuDEPP]^{2-}$. The bands at 741, 1128, and 1243 cm^{-1} are due to the δCF_3, $\nu S{-}O$, and $\nu C{-}F$ bond vibrations in the $TFSI^-$ anion, respectively.[53] The disappearance of these bands during charging is peculiar and could indicate either anion reorientation within the double layer or, perhaps, the scattering signal for these bond vibrations being hidden by intercalation in the carbon lattice. These vibration bonds of electrolyte finally reversibly convert back by the end of the discharging.

4. CONCLUSIONS

In summary, operando Raman spectroscopy and DFT calculations were employed to elucidate the overall operational mechanism of an organic full rechargeable battery composed of an organic CuDEPP anode, graphite cathode, and PP14TFSI ionic liquid electrolyte. During the electrochemical charging process two one-electron reduction reactions occurred, which changed the electronic state of the porphyrin ring and the ethynyl substituent of the CuDEPP anode, while the central Cu atom maintained its oxidation state, avoiding molecular structure collapse, whereas $PP14^+$ cations of the electrolyte migrated into the $[CuDEPP]^{2-}$ to compensate for its negative charge. To compensate for the positive charges generated on the graphite cathode, $TFSI^-$ anions intercalated into it. The discharging process was the reverse of the charging process. The full battery operated in this manner to realize its electrochemical energy storage capacity and maintain its cycling stability for thousands of cycles. The dynamic electrode processes were effectively monitored using operando Raman spectroscopy. We expect that our findings will help guide the observation, design, and optimization of the molecular structure of organic electrodes and full battery systems with improved electrochemical performances.

■ ASSOCIATED CONTENT

Supporting Information

The Supporting Information is available free of charge on the ACS Publications website at DOI: 10.1021/acs.chemmater.9b00077.

Schematic illustration of the operando electrochemical Raman spectroscopy system, UV−Vis adsorption spectrum of CuDEPP, calculation of theoretical capacity of CuDEPP, series of Raman spectra of the CuDEPP anode during initial charge−discharge cycling with a full spectral range and the corresponding potential on each spectrum, galvanostatic charge−discharge profiles and "Voltage vs cycling time" curves of the CuDEPP/PP14TFSI/graphite organic full rechargeable battery, band assignment of the Raman spectra of CuDEPP, series of Raman spectra of the graphite cathode during initial charge−discharge cycling with a full spectral range and the corresponding potential on each spectrum, and molecular structure and Raman spectrum of PP14TFSI ionic liquid electrolyte (PDF)

■ AUTHOR INFORMATION

Corresponding Authors

*E-mail: xiu-mei.lin@xmu.edu.cn (X.-M.L.).
*E-mail: dywu@xmu.edu.cn (D.-Y.W.).
*E-mail: m.fichtner@kit.edu (M.F.).

ORCID

Xiu-Mei Lin: 0000-0002-6843-2841

Notes

The authors declare no competing financial interest.

DOI: 10.1021/acs.chemmater.9b00077
Chem. Mater. 2019, 31, 3239−3247

■ ACKNOWLEDGMENTS

Financial support by EU-RTD "Hi-C" ("novel in situ and in operando techniques for the characterization of interfaces in electrochemical storage systems") in the 7th FP (grant agreement 608575) and NSFC (21775127) are gratefully acknowledged. The authors also thank Prof. Li, J. F.; Prof. Mao, B. W.; Prof. Yan, J. W.; and Dr. Tang, S. for the experimental support and helpful discussions.

■ REFERENCES

(1) Armand, M.; Tarascon, J. M. Building better batteries. *Nature* **2008**, *451*, 652−657.
(2) Song, Z.; Zhou, H. Towards sustainable and versatile energy storage devices: an overview of organic electrode materials. *Energy Environ. Sci.* **2013**, *6*, 2280−2301.
(3) Häupler, B.; Wild, A.; Schubert, U. S. Carbonyls: Powerful Organic Materials for Secondary Batteries. *Adv. Energy Mater.* **2015**, *5*, 1402034.
(4) Sun, M. H.; Huang, S. Z.; Chen, L. H.; Li, Y.; Yang, X. Y.; Yuan, Z. Y.; Su, B. L. Applications of hierarchically structured porous materials from energy storage and conversion, catalysis, photocatalysis, adsorption, separation, and sensing to biomedicine. *Chem. Soc. Rew.* **2016**, *45*, 3479−3563.
(5) Zindy, N.; Blaskovits, J. T.; Beaumont, C.; Michaud-Valcourt, J.; Saneifar, H.; Johnson, P. A.; Bélanger, D.; Leclerc, M. Pyromellitic Diimide-Based Copolymers and Their Application as Stable Cathode Active Materials in Lithium and Sodium-Ion Batteries. *Chem. Mater.* **2018**, *30*, 6821−6830.
(6) Renault, S.; Oltean, V. A.; Araujo, C. M.; Grigoriev, A.; Edstrom, K.; Brandell, D. Superlithiation of Organic Electrode Materials: The Case of Dilithium Benzenedipropiolate. *Chem. Mater.* **2016**, *28*, 1920−1926.
(7) Goodenough, J. B.; Park, K. S. The Li-Ion Rechargeable Battery: A Perspective. *J. Am. Chem. Soc.* **2013**, *135*, 1167−1176.
(8) Etacheri, V.; Marom, R.; Elazari, R.; Salitra, G.; Aurbach, D. Challenges in the development of advanced Li-ion batteries: a review. *Energy Environ. Sci.* **2011**, *4*, 3243−3262.
(9) Sk, M. A.; Manzhos, S. Exploring the sodium storage mechanism in disodium terephthalate as anode for organic battery using density-functional theory calculations. *J. Power Sources* **2016**, *324*, 572−581.
(10) Chihara, K.; Chujo, N.; Kitajou, A.; Okada, S. Cathode properties of $Na_2C_6O_6$ for sodium-ion batteries. *Electrochim. Acta* **2013**, *110*, 240−246.
(11) Wang, C.; Fang, Y.; Xu, Y.; Liang, L.; Zhou, M.; Zhao, H.; Lei, Y. Manipulation of Disodium Rhodizonate: Factors for Fast-Charge and Fast-Discharge Sodium-Ion Batteries with Long-Term Cyclability. *Adv. Funct. Mater.* **2016**, *26*, 1777−1786.
(12) Wang, Y.; Ding, Y.; Pan, L.; Shi, Y.; Yue, Z.; Shi, Y.; Yu, G. Understanding the Size-Dependent Sodium Storage Properties of $Na_2C_6O_6$-Based Organic Electrodes for Sodium-Ion Batteries. *Nano Lett.* **2016**, *16*, 3329−3334.
(13) Lee, M.; Hong, J.; Lopez, J.; Sun, Y. M.; Feng, D.; Lim, K.; Chueh, W. C.; Toney, M. F.; Cui, Y.; Bao, Z. High-performance sodium-organic battery by realizing four-sodium storage in disodium rhodizonate. *Nat. Energy* **2017**, *2*, 861−868.
(14) Song, Z.; Zhan, H.; Zhou, Y. Anthraquinone based polymer as high performance cathode material for rechargeable lithium batteries. *Chem. Commun.* **2009**, 448−450.
(15) Bitenc, J.; Pirnat, K.; Bančič, T.; Gaberšček, M.; Genorio, B.; Randon-Vitanova, A.; Dominko, R. Anthraquinone-Based Polymer as Cathode in Rechargeable Magnesium Batteries. *ChemSusChem* **2015**, *8*, 4128−4132.
(16) Vizintin, A.; Bitenc, J.; Lautar, A. K.; Pirnat, K.; Grdadolnik, J.; Stare, J.; Randon-Vitanova, A.; Dominko, R. Probing electrochemical reactions in organic cathode materials via in operando infrared spectroscopy. *Nat. Commun.* **2018**, *9*, 1−7.
(17) Baddour-Hadjean, R.; Pereira-Ramos, J. P. Raman Microspectrometry Applied to the Study of Electrode Materials for Lithium Batteries. *Chem. Rev.* **2010**, *110*, 1278−1319.
(18) Moskovits, M. Surface-enhanced Spectroscopy. *Rev. Mod. Phys.* **1985**, *57*, 783−826.
(19) Tian, Z-Q; Ren, B.; Wu, D.-Y. Surface-Enhanced Raman Scattering: From Noble to Transition Metals and from Rough Surfaces to Ordered Nanostructures. *J. Phys. Chem. B* **2002**, *106*, 9463−9483.
(20) Lu, J.; Wu, T.; Amine, K. State-of-the-art characterization techniques for advanced lithium-ion batteries. *Nat. Energy* **2017**, *2*, 17011.
(21) Sole, C.; Drewett, N. E.; Hardwick, L. J. In situ Raman study of lithium-ion intercalation into microcrystalline graphite. *J. Faraday Discuss.* **2014**, *172*, 223−237.
(22) Lin, X.-M.; Diemant, T.; Mu, X.; Gao, P.; Behm, R. J.; Fichtner, M. Spectroscopic investigations on the origin of the improved performance of composites of nanoparticles/graphene sheets as anodes for lithium ion batteries. *Carbon* **2018**, *127*, 47−56.
(23) Cohn, A. P.; Share, K.; Carter, R.; Oakes, L.; Pint, C. L. Ultrafast Solvent-Assisted Sodium Ion Intercalation into Highly Crystalline Few-Layered Graphene. *Nano Lett.* **2015**, *16*, 543−548.
(24) Goers, D.; Baertsch, M. C.; Wuersig, A.; Hardwick, L.; Novak, P. In situ Raman studies of phenolic resin based hard carbon. In *New Trends in Intercalation Compounds for Energy Storage*. Zaghib, K.; Julien, C. M.; Prakash, J. (Eds.); Springer: 2003, vol. *20*, pp. 107.
(25) Markevich, E.; Baranchugov, V.; Salitra, G.; Aurbach, D.; Schmidt, M. A. Behavior of Graphite Electrodes in Solutions Based on Ionic Liquids in In Situ Raman Studies. *J. Electrochem. Soc.* **2008**, *155*, A132−A137.
(26) Vinayan, B. P.; Diemant, T.; Lin, X.-M.; Cambaz, M. A.; Golla-Schindler, U.; Kaiser, U.; Behm, R. J.; Fichtner, M. Nitrogen Rich Hierarchically Organized Porous Carbon/Sulfur Composite Cathode Electrode for High Performance Li/S Battery: A Mechanistic Investigation by Operando Spectroscopic Studies. *Adv. Mater. Interfaces* **2016**, *3*, 1600372 (1 -10) .
(27) Chen, J.-J.; Yuan, R.-M.; Feng, J.-M.; Zhang, Q.; Huang, J.-X.; Fu, G.; Zheng, M.-S.; Ren, B.; Dong, Q.-F. Conductive Lewis Base Matrix to Recover the Missing Link of Li2S8during the Sulfur Redox Cycle in Li-S Battery. *Chem. Mater.* **2015**, *27*, 2048−2055.
(28) Qiao, Y.; Guo, S.; Zhu, K.; Liu, P.; Li, X.; Jiang, K.; Sun, C.-J.; Chen, M.; Zhou, H. Reversible anionic redox activity in Na3RuO4cathodes: a prototype Na-rich layered oxide. *Energy Environ. Sci.* **2018**, *11*, 299−305.
(29) Huang, J.-X.; Li, B.; Liu, B.; Liu, B.-J.; Zhao, J.-B.; Ren, B. Structural evolution of NM (Ni and Mn) lithium-rich layered material revealed by in-situ electrochemical Raman spectroscopic study. *J. Power Sources* **2016**, *310*, 85−90.
(30) Dokko, K.; Mohamedi, M.; Anzue, N.; Itoh, T.; Uchida, I. In situ Raman spectroscopic studies of $_{LiNixMn2}$ − xO4thin film cathode materials for lithium ion secondary batteries. *J. Mater. Chem.* **2002**, *12*, 3688−3693.
(31) Milgrom, L. R. *The Colors of Life: An Introduction to the Chemistry of Porphyrins and Related Compounds*; Oxford University Press: Oxford, 1997.
(32) Yella, A.; Lee, H.-W.; Tsao, H. N.; Yi, C.; et al. Porphyrin-Sensitized Solar Cells with Cobalt (II/III)-Based Redox Electrolyte Exceed 12 Percent Efficiency. *Science* **2011**, *334*, 629−634.
(33) Son, H.-J.; Jin, S.; Patwardhan, S.; Wezenberg, S. J.; Jeong, N. C.; So, M.; Wilmer, C. E.; Sarjeant, A. A.; Schatz, G. C.; Snurr, R. Q.; Farha, O. K.; Wiederrecht, G. P; Hupp, J. T. Light-Harvesting and Ultrafast Energy Migration in Porphyrin-Based Metal-Organic Frameworks. *J. Am. Chem. Soc.* **2013**, *135*, 862−869.
(34) Won, D.-I.; Lee, J.-S.; Ba, Q.; Cho, Y.-J.; Cheong, H.-Y.; Choi, S.; Kim, C. H.; Son, H.-J.; Pac, C.; Kang, S. O. Development of a Lower Energy Photosensitizer for Photocatalytic CO2Reduction: Modification of Porphyrin Dye in Hybrid Catalyst System. *ACS Catal.* **2018**, *8*, 1018−1030.

DOI: 10.1021/acs.chemmater.9b00077
Chem. Mater. 2019, 31, 3239−3247

(35) Gao, P.; Chen, Z.; Zhao-Karger, Z.; Mueller, J. E.; Jung, C.; Klyatskaya, S.; Diemant, T.; Fuhr, O.; Jacob, T.; Behm, R. J.; Ruben, M.; Fichtner, M. A Porphyrin Complex as a Self-Conditioned Electrode Material for High-Performance Energy Storage. *Angew. Chem. Int. Ed.* **2017**, *56*, 10341−10346.
(36) Shin, J.-Y.; Yamada, T.; Yoshikawa, H.; Awaga, K.; Shinokubo, H. An Antiaromatic Electrode-Active Material Enabling High Capacity and Stable Performance of Rechargeable Batteries. *Angew. Chem. Int. Ed.* **2014**, *53*, 3096−3101.
(37) Xu, F.; Xu, H.; Chen, X.; Wu, D.; Wu, Y.; Liu, H.; Gu, C.; Fu, R.; Jiang, D. Radical Covalent Organic Frameworks: A General Strategy to Immobilize Open-Accessible Polyradicals for High-Performance Capacitive Energy Storage. *Angew. Chem.* **2015**, *54*, 6814−6818.
(38) Yang, H.; Zhang, S.; Han, L.; Zhang, Z.; Xue, Z.; Gao, J.; Li, Y.; Huang, C.; Yi, Y.; Liu, H.; Li, Y. High Conductive Two-Dimensional Covalent Organic Framework for Lithium Storage with Large Capacity. *ACS Appl. Mater. Interfaces* **2016**, *8*, 5366−5375.
(39) Ma, T.; Pan, Z.; Miao, L.; Chen, C.; Han, M.; Shang, Z.; Chen, J. Porphyrin-Based Symmetric Redox-Flow Batteries towards Cold-Climate Energy Storage. *Angew. Chem.* **2018**, *130*, 3212−6.
(40) Yamamoto, Y.; Hirata, Y.; Kodama, M.; Yamaguchi, T.; Matsukawa, S.; Akiba, K.; Hashizume, D.; Iwasaki, F.; Muranaka, A.; Uchiyama, M.; Chen, P.; Kadish, K. M.; Kobayashi, N. Synthesis, Reactions, and Electronic Properties of 16 π-Electron Octaisobutyltetraphenylporphyrin. *J. Am. Chem. Soc.* **2010**, *132*, 12627−12638.
(41) Liao, M.-S.; Scheinera, S. Electronic structure and bonding in metal porphyrins, metal=Fe, Co, Ni, Cu, Zn. *J. Chem. Phys.* **2002**, *117*, 205−219.
(42) Sengupta, K.; Chatterjee, S.; Samanta, S.; Dey, A. Direct observation of intermediates formed during steady-state electrocatalytic O_2 reduction by iron porphyrins. *Proc. Natl. Acad. Sci. U. S. A.* **2013**, *110*, 8431−8436.
(43) Silva, C. D.; Czarnecki, K.; Ryan, M. D. Visible and resonance Raman spectra of low valent iron porphyrins. *Inorg. Chim. Acta* **1999**, *287*, 21−26.
(44) Atamian, M.; Donohoe, R. J.; Lindsey, I. J. S.; Bocian, D. F. Resonance Raman Spectra and Normal-Coordinate Analysis of Reduced Porphyrins. 1. Zinc(II) Tetraphenylporphyrin Anion. *J. Phys. Chem.* **1989**, *93*, 2236−2243.
(45) LeCours, S. M.; Philips, C. M.; Paula, J. C.; Therien, M. J. Synthesis, Transient Absorption, and Transient Resonance Raman Spectroscopy of Novel Electron Donor-Acceptor Complexes: [5,15-Bis[(4'-nitrophenyl)ethynyl]-10,20- diphenylporphinato]copper(II) and [5-[[4'-(Dimethylamino)phenyl]ethynyl]-15-[(4''-nitrophenyl)-ethynyl]-10,20-diphenylporphinato]copper(II). *J. Am. Chem. Soc.* **1997**, *119*, 12578−12589.
(46) Terner, J.; Palaniappan, V.; Gold, A.; Weiss, R.; Fitzgerald, M. M.; Sullivan, A. M.; Hosten, C. M. Resonance Raman spectroscopy of oxoiron(IV) porphyrin π-cation radical and oxoiron(IV) hemes in peroxidase intermediates. *J. Inorg. Biochem.* **2006**, *100*, 480−501.
(47) Teraoka, J.; Hashimoto, S.; Sugimoto, H.; Mori, M.; Kitagawa, T. Resonance Raman Characterization of Highly Reduced Iron Octaethylporphyrin: [Fe(OEP)]n- (n = 0, 1, and 2). *J. Am. Chem. Soc.* **1987**, *109*, 180−184.
(48) Hickman, D. L.; Shirazi, A.; Goff, H. M. Deuterium NMR Spectroscopic Studies of Low-Valent Iron Porphyrin Species. *Inorg. Chem.* **1985**, *24*, 563−566.
(49) Prathapan, S.; Johnson, T. E.; Lindsey, J. S. Building-Block Synthesis of Porphyrin Light-Harvesting Arrays. *J. Am. Chem. Soc.* **1993**, *115*, 7519−7520.
(50) Stranger, R.; McGrady, J. E.; Arnold, D. P.; Lane, I.; Heath, G. A. Communication between Porphyrin Rings in the Butadiyne-Bridged Dimer Ni(OEP)(μ-C4)Ni(OEP): A Density Functional Study. *Inorg. Chem.* **1996**, *35*, 7791−7797.
(51) Hardwick, L. J.; Ruch, P. W.; Hahn, M.; Scheifele, W.; Körtz, R.; Novák, P. *In situ* Raman spectroscopy of insertion electrodes for lithium-ion batteries and supercapacitors: First cycle effects. *J. Phys. Chem. Solids* **2008**, *69*, 1232−1237.
(52) Hardwick, L. J.; Hahn, M.; Ruch, P. W.; Holzapfel, M.; Scheifele, W.; Buqa, H.; Frank, K.; Novak, P.; Kortz, R. An in situ Raman study of the intercalation of supercapacitor-type electrolyte into microcrystalline graphite. *Electrochim. Acta* **2006**, *52*, 675−680.
(53) Paschoal, V. H.; Faria, L.; Ribeiro, M. Vibrational Spectroscopy of Ionic Liquids. *Chem. Rev.* **2017**, *117*, 7053−7112.

DOI: 10.1021/acs.chemmater.9b00077
Chem. Mater. 2019, 31, 3239−3247